JOURNAL OF APPLIED CRYSTALLOGRAPHY

ISSN: 1600-5767
journals.iucr.org/j

Real-time study of transients during high-temperature creep of an Ni-base superalloy by far-field high-energy synchrotron X-ray diffraction

Roxane Tréhorel, Gabor Ribarik, Thomas Schenk and Alain Jacques

J. Appl. Cryst. (2018). **51**, 1274–1282

JOURNAL OF APPLIED CRYSTALLOGRAPHY
ISSN 1600-5767

Real-time study of transients during high-temperature creep of an Ni-base superalloy by far-field high-energy synchrotron X-ray diffraction

Roxane Tréhorel,[a] Gabor Ribarik,[a,b,c] Thomas Schenk[a,b]* and Alain Jacques[a,b]

[a]Institut Jean Lamour, CNRS UMR 7198, Nancy, France, [b]Laboratory of Excellence on Design of Alloy Metals for Low-Mass Structures (DAMAS), Université de Lorraine, France, and [c]Department of Physics, Eötvös University, Budapest, Hungary. *Correspondence e-mail: thomas.schenk@univ-lorraine.fr

Received 9 October 2017
Accepted 11 July 2018

Edited by G. Kostorz, ETH Zurich, Switzerland

Keywords: X-ray diffraction; transmission geometry; far field; misfit; Ni-base superalloys.

The high-temperature mechanical behavior of single-crystal Ni-base superalloys has been formerly studied by *in situ* triple-crystal synchrotron X-ray diffractometry (TCD). However, the 1/300 s recording frequency does not allow real-time tests. It is shown here that real-time monitoring is possible with far-field diffractometry in transmission. The use of a far-field camera enables one to follow a diffraction spot with high angular precision and high recording speed. This technique allows measurement of the mechanical response of an AM1 Ni-base single-crystal superalloy following steep load jumps and relaxations during high-temperature creep tests. Local crystal misorientation is revealed and rafting (oriented coalescence) is examined. This new technique is compared with TCD, in order to highlight its benefits and drawbacks.

1. Introduction

X-ray diffraction is among the most effective nondestructive techniques for structural analysis and characterization of crystalline materials at atomic scale. It is usually used to identify crystalline phases, to determine residual stresses and to study defects.

The high-intensity beams provided by synchrotrons, associated with fast high-resolution detectors, now allow recording of two-dimensional diffraction patterns in a few hundredths of a second, while the construction of dedicated high-energy beamlines such as ID15, ID11 (ESRF), P07 (DESY) and 1 ID (APS) provides the hard X-ray beams necessary to investigate bulk metal specimens in transmission geometry. Thanks to the manufacture of suitable testing devices, it is now possible to follow the thermo-mechanical response of a material (*i.e.* the variations of lattice parameters) to sharp variations in stress or temperature during X-ray *in situ* experiments (Liss *et al.*, 2003).

By putting a camera in the far field, following a diffraction spot with high angular accuracy and in real time becomes possible (Kampmann *et al.*, 2001; Böhm *et al.*, 2003). The aim of this paper is to describe this double-crystal diffractometry (DCD) setup and to give some preliminary results on high-temperature creep tests with fast transients on a model material: AM1 Ni-base single-crystal superalloy (Caron & Lavigne, 2011). These results are compared with previous studies using triple-crystal synchrotron X-ray diffractometry (TCD) for similar experiments (Dirand, Cormier *et al.*, 2013; Dirand, Jacques *et al.*, 2013).

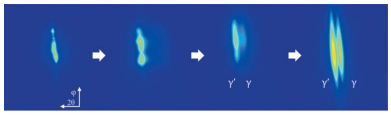

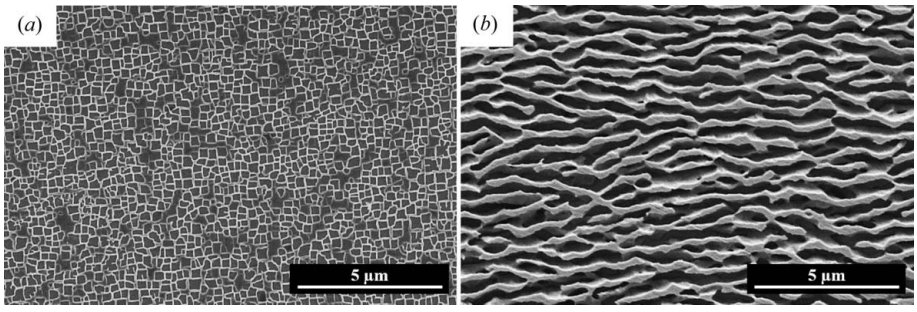

Figure 1
SEM images of the AM1 Ni-base SX superalloy (γ' dark and γ bright): (*a*) initial state after solution heat treatment and cooling in air; (*b*) after creep, stage II ([001] vertical tensile axis).

To supplement this investigation, different microscopy techniques were used to confirm observations made by X-ray diffraction. Scanning electron microscopy (SEM) was used to characterize the microstructure, electron backscatter diffraction (EBSD) to check on the orientation distribution of our samples, electron probe microanalysis (EPMA) to map some chemical elements and transmission electron microscopy (TEM) to estimate dislocation densities.

2. Studied material

2.1. Microstructure of Ni-base single-crystal superalloys

Ni-base single-crystal (SX) superalloys are used for turbine blades working at high temperature, above 1274 K, owing to their excellent creep resistance (Donachie & Donachie, 2005; Reed & Rae, 2014). This study focuses on specimens of the first-generation AM1 alloy having an approximate [001] growth orientation. After the initial heat treatment, its microstructure is characterized by a face-centered cubic γ matrix with evenly spaced coherent cuboidal $L1_2$ γ' precipitates (Fig. 1*a*). Chemical and microstructural inhomogenities exist, for instance between dendritic and interdendritic zones inherited from crystal growth.

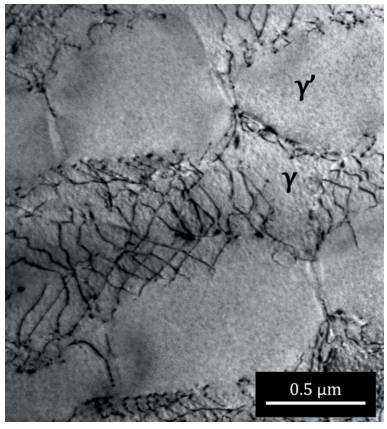

Figure 2
Post-mortem TEM image of the specimen cooled under load at the end of the experiment {[101] axis zone for **G** = (020)}, showing interface dislocations.

While the 'free' lattice parameters a^{γ} and $a^{\gamma'}$ of γ and γ' are nearly equal at room temperature, they differ at high temperature, resulting in a small (a few 10^{-3}), negative and temperature-dependent (Royer *et al.*, 1998) natural misfit $\delta(T)$ [equation (1)], which has an impact on the morphology of γ' precipitates (Donachie & Donachie, 2005) and the stress state of the microstructure:

$$\delta(T) = 2\frac{a^{\gamma'} - a^{\gamma}}{a^{\gamma'} + a^{\gamma}}. \qquad (1)$$

The high-temperature (above 1173 K) creep of nickel-base superalloys induces during stage I an oriented coalescence of the γ' precipitates, resulting in a lamellar microstructure (Fig. 1*b*).

Under tensile load and for a negative misfit, dislocations glide within the γ channels perpendicular to the [001] tensile axis (Pollock & Argon, 1994; Nabarro *et al.*, 1996; Mughrabi, 2009). These dislocations do not propagate into the γ' phase, and dislocation segments remain trapped at the γ/γ' interfaces. Internal stresses are partly relaxed by the stress field of these dislocations, whereas in γ channels parallel to the tensile axis the coherence stresses do not change. This difference in stored elastic energy is the source of rafting: the less stable vertical channels disappear while the horizontal ones thicken (Véron *et al.*, 1996; Mughrabi, 2009). The resulting γ' platelets are usually called rafts. During stage II of creep, the microstructure is similar to a composite, as shown in Fig. 1(*b*), with a $\sim 10^7$ m^{-1} density of interface dislocations accommodating the difference in plastic strain between the phases (Fig. 2).

This simple two-phase SX microstructure during creep makes the AM1 SX superalloy an ideal choice for this study.

2.2. Information needed to characterize the observed creep behavior

As shown by Dirand, Jacques *et al.* (2013) the main experimental parameters needed to investigate this mechanical behavior are the volume fraction of the γ' phase and the interface dislocation density: these dislocations introduce a mismatch $\delta_{\perp}$ (a few 10^{-3}) between the γ and γ' phases along both the **X** direction and the **Y** direction perpendicular to the [001] tensile axis, which may relax or even reverse internal stresses due to the natural mismatch $\delta(T)$:

$$\delta_{\perp} = 2\frac{a_y^{\gamma'} - a_y^{\gamma}}{a_y^{\gamma'} + a_y^{\gamma}} = \frac{b}{d}, \qquad (2)$$

where b is the magnitude of the Burgers vector of interface dislocations and d their average distance. Using a simplified layered composite model of the microstructure the internal stresses of both phases can be expressed as functions of the elastic constants and the difference between $\delta(T)$ and $\delta_{\perp}$ (Jacques *et al.*, 2004; Dirand, Jacques *et al.*, 2013). Therefore $\delta_{\perp}$

has to be deduced with a good precision from the profile of the 020 diffraction peak.

It has already been proven that TCD meets this challenge, and as we will see in §3.2, so does DCD.

However, we shall show that only DCD is useful for following fast transients. These tests are important since they can simulate one-engine-inoperative events which can be encountered during in-service operation of turboshaft engines (leading to overheating under load).

3. Experimental setups

The usual dilemma of diffraction experiments is between the precision of measurements and the acquisition frequency. The relative precision $\Delta d/d_{hkl}$ of the measurement of lattice plane distances d_{hkl} is deduced from Bragg's law by

$$\left|\Delta d/d_{hkl}\right| = |\Delta\theta|\cot(\theta). \quad (3)$$

Thus, the precision of d_{hkl} decreases with decreasing θ, or with increasing X-ray energy.

However high X-ray energies are necessary to perform bulk measurements in the Laue condition. A high-resolution technique such as TCD overcomes the weak sensitivity for lattice variations for high beam energies. It allows lattice parameter measurements with a relative precision in the 10^{-5} range (Liss *et al.*, 1998; Dirand, Jacques *et al.*, 2013). This also holds true for far-field DCD (§3.2), a setup that slightly reduces the angular resolution but has the benefit of faster acquisitions.

TCD and DCD are designed for transmission geometry. For both, the white beam is first diffracted by a tunable monochromator. Then the monochromatic beam travels through the bulk sample and diffracts under the Bragg condition. The specimens are centered in a 'home-made' high-temperature straining device (Feiereisen *et al.*, 2003) placed on the diffractometer. This allows us to perform an *in situ* creep test and simultaneously record diffraction patterns of the sample. The single-crystal sample is rotated along ω (vertical [001] tensile axis) to bring the sought (020) lattice plane into the Bragg condition with the help of a near-field camera.

3.1. TCD

The main aim of this setup (Fig. 3) is the accurate measurement of the intensity in the vicinity of a reciprocal lattice point **G** (Liss *et al.*, 1998). This setup has been used for several studies on bulk materials (Bouchard *et al.*, 1993; Seitz *et al.*, 2004). Some of these focus on the response of a specific AM1 Ni-base SX superalloy to load variations (Royer *et al.*, 1998; Diologent *et al.*, 2003; Jacques & Bastie, 2003; Jacques *et al.*, 2004, 2008; Dirand, Jacques *et al.*, 2013; Dirand, Cormier *et al.*, 2013) or to changes in temperature (le Graverend *et al.*, 2015).

TCD uses three crystals in a nondispersive (+, −, +) geometry: first a monochromator [Si(311)], then the sample and third an analyzer identical to the monochromator. In these experiments the AM1 sample is placed in the Bragg condition for **G** = (020) diffraction. Therefore, the sample has to be rotated around the vertical (Z) axis (ω rotation) and tilted along the incoming beam (φ rotation around the X axis) to put the (020) diffracted beams into the horizontal plane. Diffracted beams with slightly different directions then go through the analyzer (α angle), which selects a specific direction and diffracts the corresponding beam into a CANBERRA energy-selective Ge detector (black box in Fig. 3). The first ω rotation gives access to part of the local orientation of the diffracting planes within the material. A full scan along the **G** direction for parallel lattice planes can be recorded during a $\theta/2\theta$ scan: rotating ω and α stepwise (with double step size) with 1 s counting at each position. The result is the distribution of lattice parameters within the material (Fig. 4 and Table 1).

At each ω, α position the analyzer selects within the probed sample diffracting planes with a well defined plane spacing. However, since this TCD setup is ill collimated in Z (5 mm vertical detector gap and no Soller slits), the recorded intensity includes contributions from beams tilted by a small angle $\Delta\varphi$ along the incoming beam, *i.e.* from slightly tilted lattice planes. The experiments were conducted at 120 keV (λ = 1.033×10^{-11} m) at DESY BW5 (Bouchard *et al.*, 1998). The cylindrical specimen had 3.4 mm diameter, and the volume probed by the synchrotron beam was 0.05 mm (vertical slits) × 0.05 mm (horizontal slits) × 3.4 mm, which is sufficient to probe both dendritic and interdendritic zones. The large

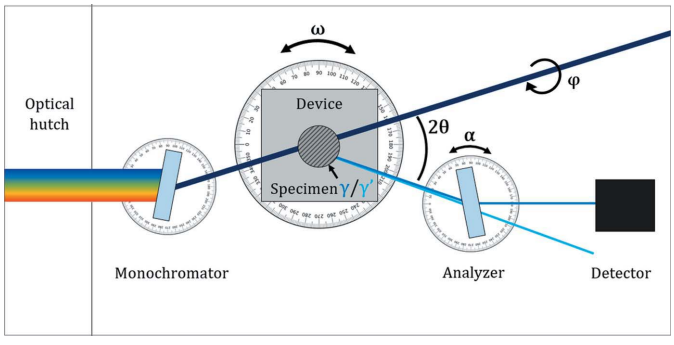

Figure 3
Setup of a triple-crystal diffractometer.

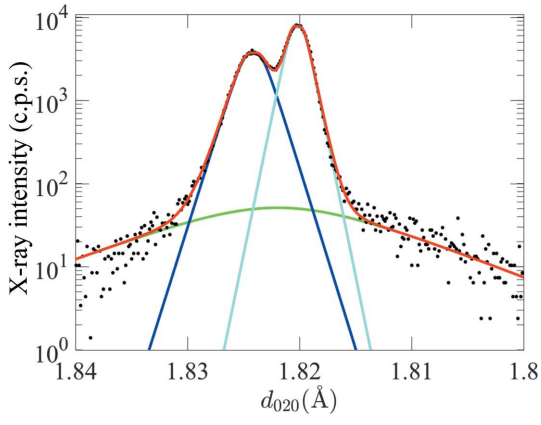

Figure 4
TCD $\theta/2\theta$ scan of the 020 reflection for an Ni-base single-crystal superalloy after rafting on BW5 at 120 keV; further details in Table 1 (Dirand, Jacques *et al.*, 2013).

Table 1
Parameters of used experiment methods, TCD and DCD (see text).

	TCD	DCD far field
Energy	120 keV	67 keV
Detector	Germanium crystal, 1.5 cm thick	FreLoN camera, 2048 × 2048, 50 × 50 µm pixel size
Detector slits	5 × 5 mm	–
Sample diameter	3.4 mm	2 mm
Volume traversed by X-rays	0.0085 mm^3	0.02 mm^3
Peak intensity	$\sim 10^4$	$\sim 10^4$
Accuracy of $\delta_\perp$ after fit	$\sim 10^{-5}$	$\sim 10^{-5}$
Acquisition time	5 min	7 s

vertical (Z) slit gap results in a maximum beam intensity of typically 7000 counts per second. This is within the linear range of the detector, and with careful screening, the background count is less than one count per second. A 200 point analyzer scan by TCD (1″ α step) lasts about 300 s: the high resolution in reciprocal space is achieved at the cost of the long (though much shorter than with a laboratory X-ray source) recording time necessary to count the diffracted beam intensities at successive ω and α positions. The resulting profiles are fitted with three peaks (γ, γ' and background) defined as (Jacques & Bastie, 2003)

$$F(x) = A \exp\left\{1 - \left[1 + \left(\frac{|x - x_0|}{w}\right)^{\beta}\right]^{1/\beta}\right\}. \qquad (4)$$

The factor A is the peak height, β represents the curvature of the top of the peaks, $1/w$ corresponds to the slope of the peaks in logarithmic scale and x_0 is the peak center. The ratio of the γ/γ' peak areas gives the volume fraction with a small correction factor, as the scattering amplitude for the (020) planes is 1.5% lower for γ than for γ' (Jacques, 2016). The w slope is related to the density of dislocations according to theory (Ungár *et al.*, 1993) and recent simulations (Jacques, 2016).

As the peaks are well separated, both γ and γ' lattice parameters can be extracted and then $\delta_\perp$ can be determined. After peak fitting, the absolute precision of the angular distance between the two peaks is 0.1″, and the $\Delta 2\theta/\theta$ precision is a few 10^{-5}.

3.2. DCD

For DCD a near-field camera is first moved into the diffraction cone of the sample. Each reflection gives a sharp spot on the camera (Fig. 5). The specimen is rotated along ω to find the maximum intensity of the 020 diffraction spot. The near-field camera is then moved out of the diffracted beam alignment.

By putting a similar camera in the far field it becomes possible to record a high-resolution image of the diffraction spot (Kampmann *et al.*, 2001; Böhm *et al.*, 2003) and to resolve the angular difference between the γ and γ' peaks (Fig. 6).

The experiments were done at ESRF ID11, with an Si(111) monochromator. The choice of 67 keV radiation energy (λ = 1.851×10^{-11} m), below the W and Ta absorption edges, resulted from a compromise between the efficiency of the beamline wiggler, the transmission through the specimen and the photon-conversion yield of the camera. The cylindrical specimens were 2 mm in diameter. The probed volume was 200 µm (vertical) × 50 µm (horizontal) × 2 mm and the detector was a two-dimensional 2048 × 2048 pixel FReLoN camera with a pixel size of 50 × 50 µm.

Owing to the limited hutch dimensions, the furthest that the camera could be placed from the specimen was 8.5 m. It was shifted by ∼0.85 m from the incident beam in the horizontal plane (2θ angle). As the [001] direction of the sample is not perfectly parallel to the vertical tensile (Z) axes of the specimen, the diffracted beam does not lie in the horizontal plane and the far-field camera was shifted ∼0.1 m vertically to center the diffracted beam and to accommodate the 6.5° φ angle between the [001] direction and the vertical specimen axis. Parallel diffracted beams coming from the entry and exit faces of the specimen will be shifted by four pixels. Moreover, as the distance from the camera to the incident beam cannot be determined with a precision better than 1 mm, the absolute precision of the peak positions is about 10^{-3}. However, the raw relative precision in peak shifts due to changes in temperature or stresses, as well as the distance between the γ and γ' peaks, is one pixel (*i.e.* 10^{-4}) and can be improved by peak fitting to 10^{-5}, as precise as TCD.

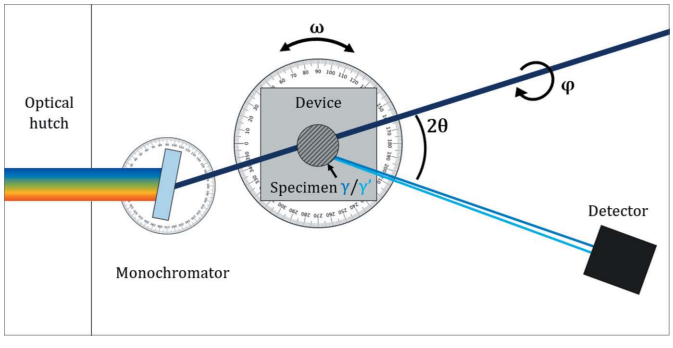

Figure 5
Far-field double-crystal diffractometer setup. A near-field FReLoN camera is used to find the 020 reflection and the approximate position of the diffraction spot, which is then followed with the far-field FReLoN camera.

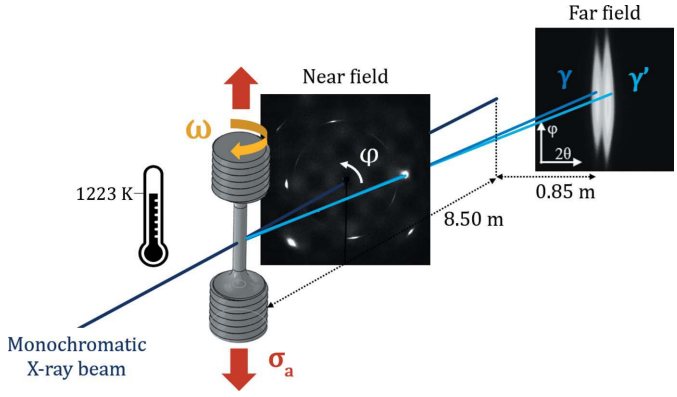

Figure 6
Far-field DCD setup.

With this experimental setup we recorded two different types of integrated diffraction images, namely three-dimensional scans and fully integrated images. During three-dimensional scans, the whole ω range of the reflection ($\sim$2.6°) was divided into $\Delta\omega = 0.05°$ scans, and one integrated image was recorded during each scan. Such image sequences can be recorded in only 40 s (acquisition times depend on the rotation angle/number of images taken for the set) and give a complete view of a diffraction profile according to the different angles 2θ, φ and ω.

Fully integrated images were obtained by sweeping the whole ω range of the reflection in one scan (two-dimensional scans) and could be recorded in 7 s. Regions of interest (ROIs) covering 800 × 800 pixels were extracted from the initial images after background deduction [200 counts per second (c.p.s.)]. They could then be used for qualitative analysis or rotated by $\Delta\varphi$ (6.5°) to put the reflection virtually in the horizontal (diffraction and camera) plane for further analysis. As the maximum intensity on a pixel line was $\sim$7000 c.p.s. the images below are shown in logarithmic scale in order to make the tails of the peaks clearly visible.

To summarize, a $\theta/2\theta$ TCD scan records the peak profile along a reciprocal lattice point **G** for one fixed grain orientation, and integrates the intensity along the vertical direction (or φ), while a two-dimensional far-field DCD scan integrates the intensity along ω (all grain orientations) and plots it against 2θ and φ.

4. Experiments

4.1. Sample preparation

The cast AM1 samples were annealed at 1573 K for 3 h and air quenched with a 10 K s^{-1} cooling rate. The resulting γ' precipitates are cubic with an average size of 250 nm (Fig. 1*a*). Such a specimen was used for DCD measurements. The TCD specimens were further submitted to a 'standard' heat treatment (Fredholm *et al.*, 1985) to obtain well defined cuboidal γ' precipitates with 380 nm size.

4.2. Test course

The specimens were pre-crept (*in situ* or *ex situ*) in order to obtain a well formed rafted microstructure, and then crept at 1223 K and submitted to load jumps. After the tests, they were cooled under load and post-mortem analysis by electron microscopy was performed. The timeline in Fig. 7 summarizes the experiments conducted by DCD and TCD.

4.3. Microscopy

For SEM analysis the samples were mechanically polished and then etched for 15 s with a solution of 66% HCl and 33% HNO_3, which reveals γ as bright and γ' as dark (Fig. 1). Particle sizes were determined using the intercept method on SEM images taken by a Philips XL30 S FEG with a TLD detector at 20 kV. High-resolution surface orientation maps (1.5 µm steps) were obtained by EBSD using an FEI QUANTA 600 FEG scanning electron microscope at 20 kV. Qualitative element mapping was done by EPMA with a JEOL JXA 8530-F at 20 kV and a 200 nA current. (201) thin foils were prepared by mechanical polishing then ion beam thinning and observed with a Philips CM 200 transmission electron microscope with a high-voltage source of 200 kV.

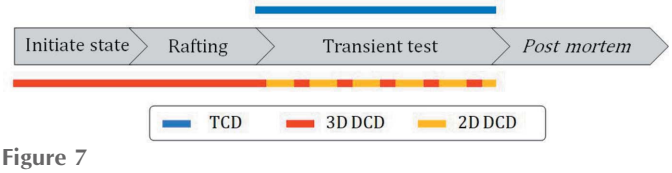

Figure 7
Test courses of DCD (red/yellow) and TCD (blue) experiments

5. Three-dimensional DCD scans results

5.1. Initial state

A three-dimensional scan is a series of two-dimensional images taken at different successive ω angles and yields a three-dimensional view of the peak profile. Results for the initial state of the specimen at room temperature are detailed in Fig. 8. Twenty images were taken at angles ω between 7.025 and 7.975° with a 0.05° angular step around the 020 reflection. Logarithms of intensity *versus* 2θ, φ position on the detector are plotted with a colored intensity scale (red: maximum).

For every recorded angle ω, various spots can be distinguished at different φ angles and slightly different 2θ angles: the specimen is not a perfect single crystal, and orientation differences between subgrains have been observed, mainly between dendritic and interdendritic zones (Kuhn *et al.*, 1991; Brückner *et al.*, 1997). Such groups of 20 (40) images are not a convenient format to compare data with those obtained by EBSD. From these 20 (40) images we build a unique plot with φ on the Y axis and ω on the X axis. Each original scan is integrated along 2θ to obtain a one-dimensional diffraction pattern along φ for one ω position. By interpolation it is possible to construct φ/ω plots, as shown in Fig. 9.

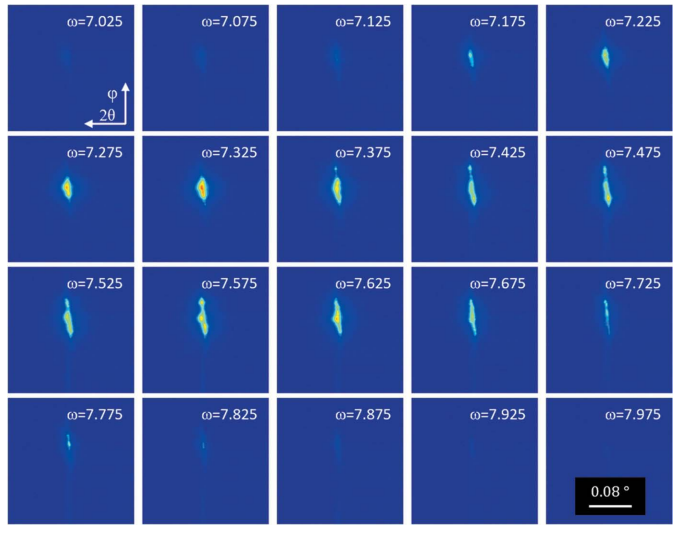

Figure 8
Three-dimensional scan of the 020 peak of the specimen in its initial state at room temperature (logarithmic intensity color plots).

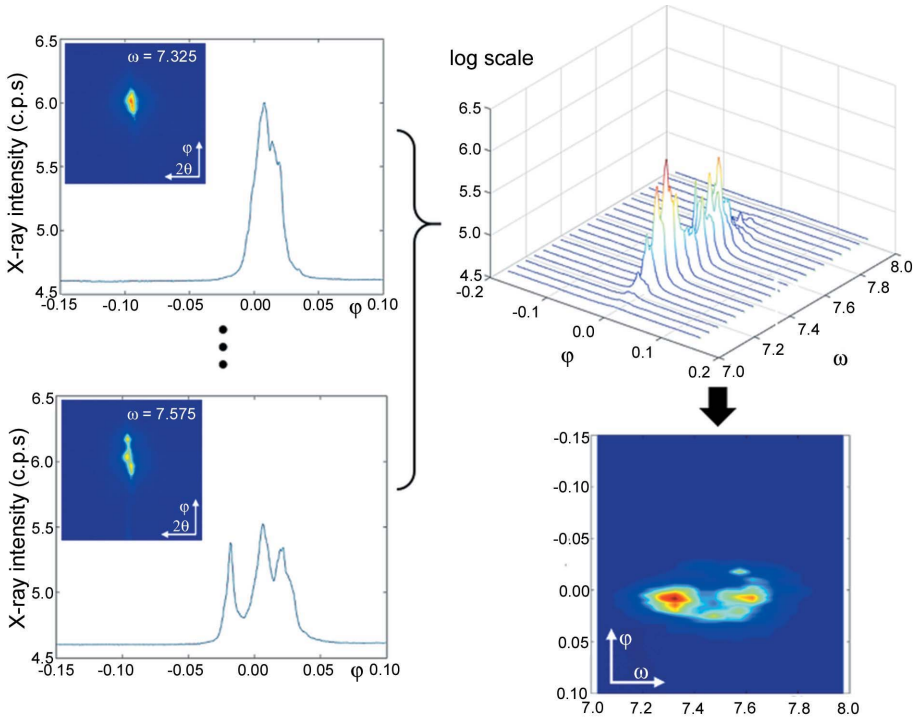

Figure 9
Construction of a φ/ω plot from three-dimensional scans of the samples' initial state at room temperature.

This plot shows several well defined spots, corresponding to a group of subgrains diffracting with slightly different φ/ω angles (Kuhn *et al.*, 1991; Bouchard *et al.*, 1993). The angular dispersion is less than 0.1° (φ) and 1° (ω). Fig. 10 shows the evolution of a φ/ω plot from initial conditions at room temperature (a) to 1223 K (b), after 30 min at 1223 K (c), and during rafting after 8 h creep at 200 MPa (d).

While the plot in Fig. 10(a) is quite sharp, it looks increasingly blurred in the following images. As the magnitude of the lattice mismatch increases with temperature from 0 to −0.0035, it generates internal stresses within the microstructure between the γ and γ' phases and between dendritic and interdendritic areas. These stresses change the local lattice parameters (blurring along $2\theta_B$) and the local plane orientation (blurring along ω and φ). They are rather homogeneous within the cuboids and the channels but vary rapidly near the edges and corners of the cuboids. Later, as the interfaces become semi-coherent, the strain field of interface dislocations adds sharp local variations which further increase the blurring. The ∼−0.2° shift of the mean ω angle between Figs. 10(a) and 10(b) is ten times larger than half the ∼3.5 × 10^{-2}° variation of the $2\theta_B$ angle between room temperature and the test temperature: we suppose this results from step losses by the motor controlling the ω rotation. Loading the specimen between Figs. 10(c) and 10(d) results in a shift along φ. (But this difference also results partially from a shift of the specimen relative to the beam due to thermal expansion of the testing device, and therefore we changed the observed sample region, impeding a detailed interpretation of the evolution of these φ/ω.) However, the spread of ω angles of the subgrains gets smaller with time (Fig. 10). This could be due to a decrease of tilt angles between columnar subgrains during creep.

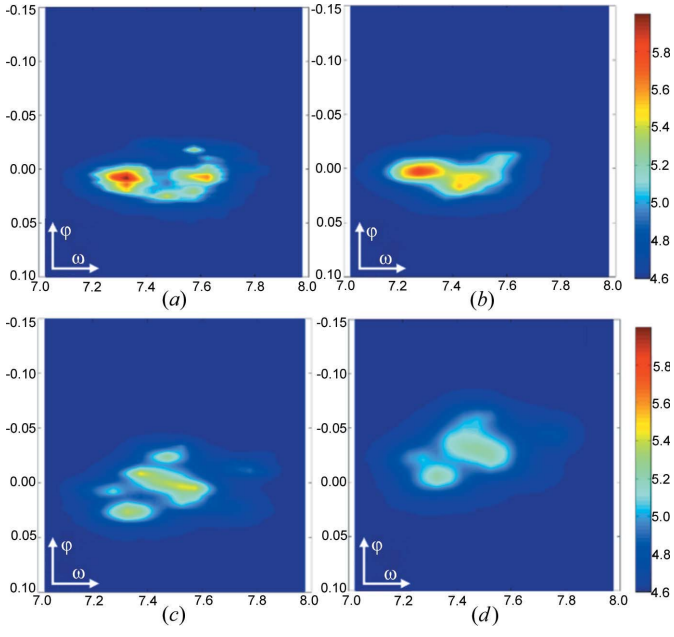

Figure 10
φ/ω plots of sample: (a) at initial state at room temperature, (b) first plot at 1223 K, (c) 30 min at 1223 K and (d) 8 h under creep conditions (1223 K at 200 MPa).

All changes can be observed within the chosen ROI ($\varphi/2\theta$) of 800 × 800 pixels. The results show that the far-field DCD setup is powerful enough to follow the evolution of the position of the peak and its profile during an *in situ* test. However, care has to be taken to always probe the same zone of the specimen.

5.2. Comparison with other investigation methods

The post-mortem EPMA maps for different elements show a partition of alloying elements between dendritic and interdendritic areas (Parsa *et al.*, 2015). Such differences in concentration cause variations both in the local fraction of γ' precipitates and in the average lattice parameter. The latter explains part of the $2\theta_B$ shifts between different group of subgrains revealed by three-dimensional DCD scans. EBSD shows, as also found by Ram *et al.* (2016), local misorientations between adjacent subgrains in the 0.5° range. Three-dimensional DCD scans thus provide new information in two ways:

(a) the mosaicity within the specimen and (b) the local misorientation within groups of subgrains which increases during the test, as shown by the blurring of the individual spots.

6. Two-dimensional scan results

6.1. Rafting

The specimen's rafting was followed continuously using two-dimensional scans, as transient tests began only when the second stage of the creep test (specimen with a lamellar microstructure) was well established.

At room temperature (Fig. 11a), several spots are visible and demonstrate the presence of subgrains as already discussed. At 1223 K (Fig. 11b), as the microstructure is still cuboidal, the peak develops a tail on the low $2\theta_B$ side, *i.e.* for larger lattice parameters: the 2θ profile is the same as for TCD scans at high temperature (Diologent *et al.*, 2003). The tail results from the elastic strain in the [010] direction of the γ channels perpendicular to [010]. After 8 h of creep (Fig. 11c), the tail resolves into a distinct second peak. As rafting is in progress, the microstructure becomes lamellar, and γ and γ' layers are no longer coherent: their (001) interfaces are overlaid by an increasing dislocation density, resulting in an increasing distance between the peaks (Dirand, Cormier *et al.*, 2013). Ten hours later and after a stress increase and decrease, rafting is well established (Fig. 11d), and two similar peaks with different intensities are clearly distinguishable. They appear as thin streaks along the φ direction, which explains the blurring along φ observed in Fig. 10(d). Simulations in progress according to Jacques (2016) suggest that this increase in φ direction of both peaks results from the increased distortion of the channels and rafts near the interface by interfacial dislocations.

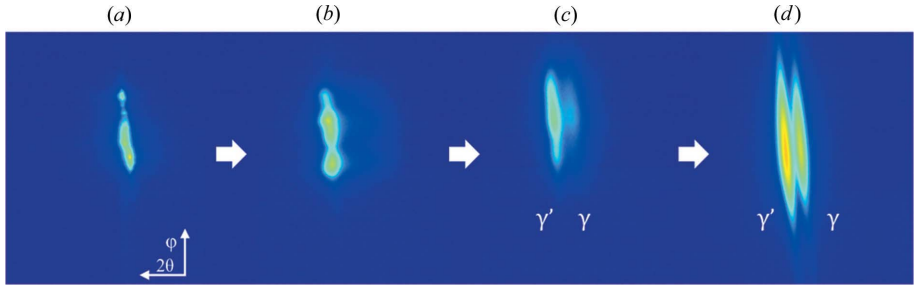

Figure 11
Rafting: two-dimensional integrated scans by DCD (ROI 800 × 800 pixels): (a) initial state, (b) 1223 K, (c) 8 h of creep and (d) 18 h of creep.

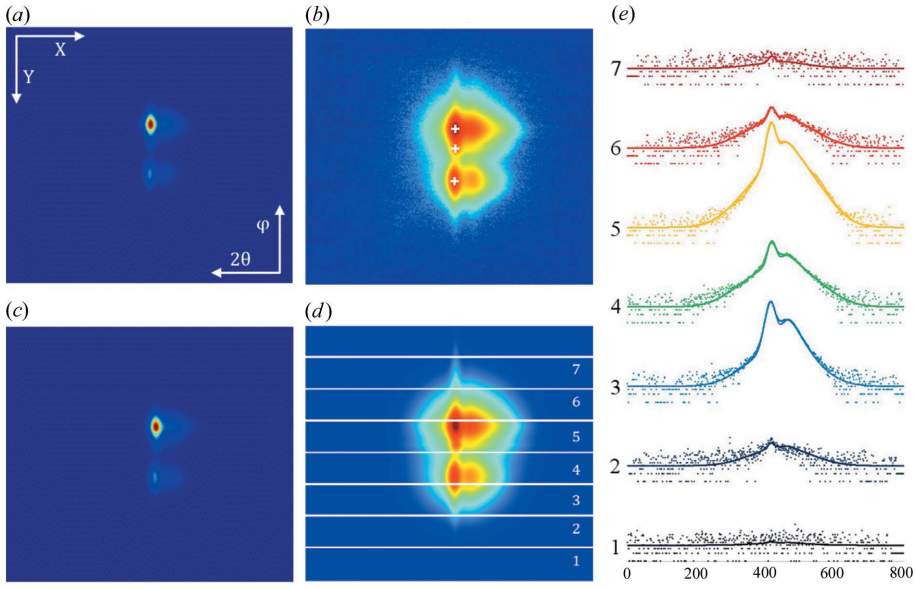

Figure 12
(a)–(d) 800 × 800 pixel ROI of an integrated image: rotated experimental (a), (b) and fitted (c), (d) images in linear (a), (c) and logarithmic (b), (d) scales; (e) logarithmic plots of horizontal lines 100–700.

6.2. One- and two-dimensional fits of the integrated images

Figs. 12(a) and 12(b) show an ROI of an integrated two-dimensional image recorded during rafting: the peaks are nearer and less distinct than in Fig. 11(c). The image was rotated through an angle $\Delta\varphi$, so that the X (Y) axis is parallel to 2θ (φ). A full analysis of the data recorded in the three- and two-dimensional images seen above would require three-dimensional fits with well chosen functions and a large amount of CPU time. We describe here a first test with the intensity plot (Figs. 12c–12d) taken as the sum of three overlapping spots (*i.e.* three groups of subgrains; white crosses are used to show the positions of the maxima of the spots, since the patterns of two of the groups are too close to be distinguished and overlap to lead to the intense upper spot on the figure). Each spot is the sum of two peaks, γ, γ', and an isotropic diffuse background (as the camera does not discriminate the photon's energy, this probably includes inelastic scattering) with an intensity proportional to that of the γ and γ' peaks. Each peak was taken as

$$I(X, Y) = f_X(X)\left[I f_{Y1}(Y) + I_S f_{Y2}(Y)\right] + I_{Bg} f_{Bg}\left[(X^2 + Y^2)^{1/2}\right], \quad (5)$$

where X and Y indicate the pixel's position on the ROI [pixel (1,1) is at the top left of the image]. All f functions have the same form as in equation (4). I is the maximum of the peak, I_S that of the top of the streaks along Y and I_{Bg} the background intensity.

Comparison of the two-dimensional plots in linear and logarithmic scale, as well as the one-dimensional linear plots

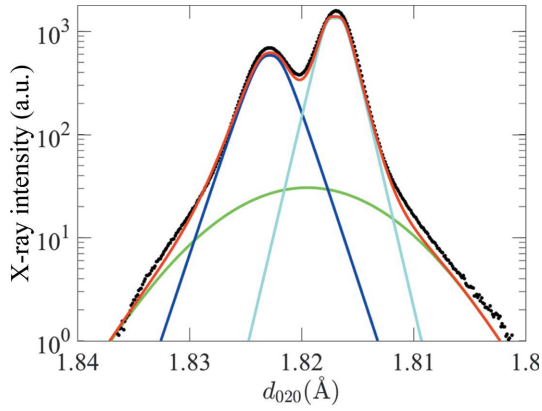

Figure 13
One-dimensional logarithm diffraction peaks from two-dimensional DCD scans: light blue for γ' peak, dark blue for γ peak, green for background and red for their sum.

(Fig. 12*e*) taken every 100 pixels, shows that a good fit can be obtained over four orders of magnitude. While giving new information on the two-dimensional and even three-dimensional structure of the diffraction spot, such fits have a high computing cost because of their slow convergence: they can be used to assess the blurring of the images and the evolution of the streaks on selected images, but not to measure the distance between peaks on the ~4000 images recorded during a single creep test. As stated above, it was more efficient to fit one-dimensional integrated plots obtained by summing the intensities of pixels along the Y (φ) direction. Thus, a profile such as that shown in Fig. 13 results from all zones illuminated by the X-ray beam and is more typical of the whole microstructure than the profile from a single subgrain.

We employed an automated fitting procedure based on MATLAB and Fortran programmed routines using the same procedure as for TCD peaks [equation (4)]. The one-dimensional profiles are nearly identical to those obtained by TCD (Fig. 4). The main difference lies in the overall intensity and the 200 c.p.s. noise of the CCD camera.

6.3. Peak evolution during stress jumps: comparison with TCD

The main goal of the experiment was to measure the variations of $\delta_\perp$, the perpendicular mismatch between the two phases during fast transients. Fig. 14(*a*) shows a 90 min subset of our data (from fits of one-dimensional DCD profiles) during which the applied load was successively increased from 200 to 250 MPa, then increased to 280 MPa, and finally decreased to its initial value. An increase of the load results in a burst of plastic strain within the γ channels, an increase of the dislocation density at the γ/γ' interfaces, and thus a decrease of the algebraic value of $\delta_\perp$, as observed *via* TCD by Dirand, Jacques *et al.* (2013); this behavior is reported in Fig. 14(*b*).

$\delta_\perp$ obtained *via* DCD evolves in the same way as that by TCD. But one point is recorded every 7 s by far-field DCD instead of every 5 min by TCD. The blue boxes in Fig. 14 show such a 5 min span during an increase of the load. During this span, not only does $\delta_\perp$ vary, but also in TCD the γ' peak is recorded about 45 s after the γ peak. This results in a blurring of the peaks and a systematic shift of their distance. A fast load jump during the recording of a 7 s image would at worst result in a blurring of the peaks and a single lost image.

However, the plot of $\delta_\perp$ in Fig. 14(*a*) exhibits a sharp -2×10^{-4} (three pixel) jump during the partial unloading of the specimen. The mobile rod of the tensile device is above the specimen and it moved 50 µm during unloading. The unloading resulted in a 25 µm (one-eighth of the slits' height) downwards shift of the specimen with respect to the X-ray beam's position. Thus, before and after unloading, the beam probed slightly different areas of the specimen, as also seen during heating in Figs. 10(*b*) and 10(*c*).

Knowing the evolution of perpendicular misfit in real time, particularly during transients, provides new information on the physical mechanisms of plasticity within both phases of Ni-base SX superalloys.

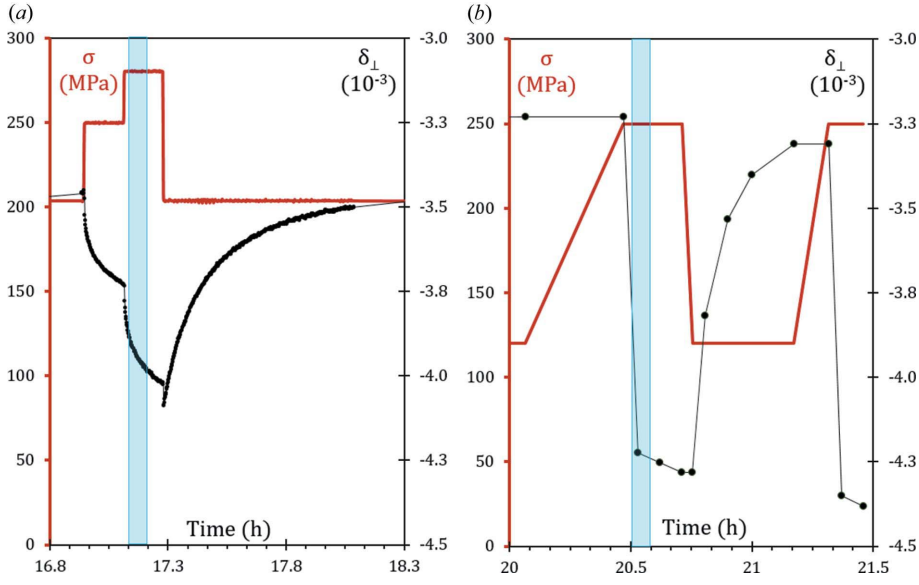

Figure 14
Plots of applied stress σ and $\delta_\perp$ estimated according to the time of *in situ* experiments for (*a*) DCD and (*b*) TCD (Dirand, Jacques *et al.*, 2013; Dirand, Cormier *et al.*, 2013).

7. Summary and conclusions

In the present work, we investigated specimens of AM1 Ni-base single-crystal superalloy during *in situ* creep tests. We used a new experimental far-field double-crystal diffractometry setup with synchrotron radiation to precisely record 020 γ and γ' diffraction patterns. This setup is compared with the triple-crystal diffractometry

technique. From the results obtained with DCD, the following conclusions can be made:

(*a*) With far-field DCD two different acquisition methods for diffraction patterns are available:

(i) two-dimensional integrated images ($\varphi/2\theta$) taken while sweeping around ω within 7 s or

(ii) three-dimensional scans, a set of series of two-dimensional images integrated along a shorter ω span (typically 0.05°).

(*b*) All measurements (the position of the peak *etc.*) obtained with TCD can also be obtained with far-field DCD without appreciable loss of resolution.

(*c*) Additionally, we obtain supplementary information with two-dimensional and three-dimensional scans on the distribution of orientations in φ and ω.

(*d*) The reduced measuring time allows following fast transients.

(*e*) Two-dimensional and three-dimensional far-field DCD images yield further information on the distribution of misorientations along φ and ω, at the cost of longer peak fitting.

(*f*) The choice to work with narrow slits (one pixel wide and four pixels high) improves the resolution. However, it decreases the statistical value of the data and carries the risk of changing the probed area upon loading or heating of the specimen. Those difficulties may be alleviated by slightly increasing the slit size, and even more by the use of a tensile device with two mobile rods moving in opposite directions, to keep the center of the specimen at a constant position.

Far-field DCD has great potential in terms of speedy acquisition of two- and three-dimensional diffraction patterns with good resolution in reciprocal space and in time.

Hence, far-field DCD can be used to follow tests on other crystalline materials using both two-dimensional and three-dimensional scans for applications needing real-time measurement. There are plenty of other applications on single crystals, such as creep, cyclic tests and fatigue, to access information including lattice parameters, lattice bending, strain, stress and mosaicity *in situ* and in real time.

Acknowledgements

The authors acknowledge Jonathan Wright, Vadim Diadkin and ESRF staff for help at the ID 11 beamline. They are grateful to Jonathan Cormier for providing specimens, Olivier Ferry for help with the high-temperature mechanical testing device and Christine Gendarme for EPMA experimentation. They would like to thank Nathalie Gey from LEM3 (Metz, France) for the collaboration about EBSD analysis. Lucile Dezerald and Pierre Bastie are gratefully acknowledged for their help during the execution of *in situ* tests.

Funding information

GR gratefully acknowledges the support of the Janos Bolyai Research Fellowship of the Hungarian Academy of Sciences.

References

Böhm, J., Wanner, A., Kampmann, R., Franz, H., Liss, K. D., Schreyer, A. & Clemens, H. (2003). *Nucl. Instrum. Methods Phys. Res. B*, **200**, 315–322.

Bouchard, R., Hupfeld, D., Lippmann, T., Neuefeind, J., Neumann, H.-B., Poulsen, H. F., Rütt, U., Schmidt, T., Schneider, J. R., Süssenbach, J. & von Zimmermann, M. (1998). *J. Synchrotron Rad.* **5**, 90–101.

Bouchard, R., Kouptsidis, S., Neumann, H. B., Schmidt, T. & Schneider, J. R. (1993). *J. Appl. Phys.* **73**, 3680–3684.

Brückner, U., Epishin, A. & Link, T. (1997). *Acta Mater.* **45**, 5223–5231.

Caron, P. & Lavigne, O. (2011). *Aerospace Lab*, **3**, AL03-02. http://www.aerospacelab-journal.org/al3/Recent-Studies-at-Onera-on-Superalloys-for-Single-Crystal-Turbine-Blades.

Diologent, F., Caron, P., d'Almeida, T., Jacques, A. & Bastie, P. (2003). *Nucl. Instrum. Methods Phys. Res. B*, **200**, 346–351.

Dirand, L., Cormier, J., Jacques, A., Chateau-Cornu, J. P., Schenk, T., Ferry, O. & Bastie, P. (2013). *Mater. Charact.* **77**, 32–46.

Dirand, L., Jacques, A., Chateau-Cornu, J., Schenk, T., Ferry, O. & Bastie, P. (2013). *Philos. Mag.* **93**, 1384–1412.

Donachie, M. J. & Donachie, S. J. (2005). *Van Nostrand's Scientific Encyclopedia*, 2nd ed. Hoboken: John Wiley and Sons.

Feiereisen, J. P., Ferry, O., Jacques, A. & George, A. (2003). *Nucl. Instrum. Methods Phys. Res. B*, **200**, 339–345.

Fredholm, A., Khan, T., Theret, J. & Davidson, J. H. (1985). Patent No. EP 0 149 942 B1.

Graverend, J. le, Jacques, A., Cormier, J., Ferry, O., Schenk, T. & Mendez, J. (2015). *Acta Mater.* **84**, 65–79.

Jacques, A. (2016). *Metall. Mater. Trans. A*, **47**, 5783–5797.

Jacques, A. & Bastie, P. (2003). *Philos. Mag.* **83**, 3005–3027.

Jacques, A., Diologent, F. & Bastie, P. (2004). *Mater. Sci. Eng. A*, **387–389**, 944–949.

Jacques, A., Diologent, F., Caron, P. & Bastie, P. (2008). *Mater. Sci. Eng. A*, **483**, 568–571.

Kampmann, R., Lippmann, T., Burmester, J., Dos Santos, J., Franz, H., Haese-Seiller, M. & Marmotti, M. (2001). *Nucl. Instrum. Methods Phys. Res. A*, **467–468**, 1261–1264.

Kuhn, H. A., Biermann, H., Ungár, T. & Mughrabi, H. (1991). *Acta Metall. Mater.* **39**, 2783–2794.

Liss, K.-D., Bartels, A., Schreyer, A. & Clemens, H. (2003). *Textures Microstruct.* **35**, 219–252.

Liss, K.-D., Royer, A., Tschentscher, T., Suortti, P. & Williams, A. P. (1998). *J. Synchrotron Rad.* **5**, 82–89.

Mughrabi, H. (2009). *Mater. Sci. Technol.* **25**, 191–204.

Nabarro, F. R., Cress, C. M. & Kotschy, P. (1996). *Acta Mater.* **44**, 3189–3198.

Parsa, A. B., Wollgramm, P., Buck, H., Somsen, C., Kostka, A., Povstugar, I., Choi, P. P., Raabe, D., Dlouhy, A., Müller, J., Spiecker, E., Demtroder, K., Schreuer, J., Neuking, K. & Eggeler, G. (2015). *Adv. Eng. Mater.* **17**, 216–230.

Pollock, T. M. & Argon, A. S. (1994). *Acta Metall. Mater.* **42**, 1859–1874.

Ram, F., Li, Z., Zaefferer, S., Hafez Haghighat, S. M., Zhu, Z., Raabe, D. & Reed, R. C. (2016). *Acta Mater.* **109**, 151–161.

Reed, R. C. & Rae, C. M. F. (2014). *Physical Metallurgy*, 5th ed., edited by D. E. Laughlin & K. Hono, pp. 2215–2290. Oxford: Elsevier.

Royer, A., Bastie, P. & Veron, M. (1998). *Acta Mater.* **46**, 5357–5368.

Seitz, C., Weisser, M., Gomm, M., Hock, R. & Magerl, A. (2004). *J. Appl. Cryst.* **37**, 901–910.

Ungár, T., Biermann, H. & Mughrabi, H. (1993). *Mater. Sci. Eng. A*, **164**, 175–179.

Véron, M., Bréchet, Y. & Louchet, F. (1996). *Acta Mater.* **44**, 3633–3641.